International Journal of Hydrogen Energy 62 (2024) 591–600

Contents lists available at ScienceDirect

International Journal of Hydrogen Energy

journal homepage: www.elsevier.com/locate/he

Numerical investigation of effect of mechanical compression on the transport properties of fuel cell microporous layer using a pore-scale model

Heng Zhang [a], Hao Hu [b], Mrittunjoy Sarker [c], Xuanyu Shao [d], Zhigang Zhan [d], Pang-Chieh Sui [e], Po-Ya Abel Chuang [c,*]

[a] School of Low-Carbon Energy and Power Engineering, China University of Mining and Technology, Xuzhou, 221116, China
[b] Automobile Technology and Service College, Wuhan City Polytechnic, Wuhan, 430064, China
[c] Mechanical Engineering, University of California, Merced, Merced, CA, 95343, USA
[d] State Key Laboratory of Advanced Technology for Materials Synthesis and Processing, Wuhan University of Technology, Hubei, 430070, China
[e] Institute for Integrated Energy Systems & Dept. of Mech. Eng., University of Victoria, Victoria, BC, V8W 2Y2, Canada

ARTICLE INFO

Handling Editor: Umit Koylu

Keywords:
PEMFC
MPL
Stress and strain
Mechanical compression
Transport properties
Pore scale model

ABSTRACT

The microporous layer (MPL) plays an important role in water and thermal management of proton exchange membrane fuel cells (PEMFCs). An in-depth investigation of the mechanical compression effect on transport properties in the MPL can help optimize cell performance. In this work, the microstructure of the MPL is numerically reconstructed and the finite element method is applied to simulate mechanical behavior. Besides, the distribution of stress-strain, porosity, and pore size in the MPL under ten different levels of mechanical compression strains are studied. Lastly, the pore-scale model is employed to investigate the effective transport properties of the MPL as a function of compression strain. The analysis reveals that as the MPL strain increases from 0% to 40%, there is a 29% decrease in porosity, a 50% reduction in average pore diameter, a 60% decrease in effective gas diffusivity, a 100% increase in tortuosity, and an 80% increase in electrical and thermal conductivity. With the escalation of mechanical compression, both the magnitude and uniformity of stress-strain-displacement concurrently rise. Mechanical compression strains below 20% exhibit a lesser impact on transport properties. Beyond this threshold, exceeding the 20% compression strain point, mechanical stress assumes a critical role in influencing MPL transport properties.

1. Introduction

To help achieve the goal of carbon neutrality, a proton exchange membrane fuel cell (PEMFC) can play an active role by converting the chemical energy of reactants into electrical energy through electrochemical reactions, without producing harmful emissions [1]. The membrane electrode assembly (MEA) is the core component of a PEMFC, comprising a gas diffusion layer (GDL), microporous layer (MPL), catalyst layer (CL), and proton exchange membrane (PEM) [2,3]. The MPL serves critical functions, providing mechanical support to PEM and CL, reducing contact resistance between GDL and CL, and enhancing the water management capability of the fuel cell. Additionally, the MPL plays a significant role in heat and mass transfer [4–7]. While there has been extensive study on the deformation of the GDL in the MEA during cell assembly, limited research has been conducted on the mechanical stress in MPL due to its thinness and mechanical fragility. Despite its small thickness, the MPL experiences significant temperature and oxygen concentration gradient, especially under higher current density situations. Furthermore, MPL deformation under mechanical stress affects the internal transport properties and consequently cell performance [6,8].

An in-depth understanding of the microstructural properties of an MPL is essential for a systematic investigation of its transport properties. Deng et al. [9], Yu et al. [4], and Hannach et al. [10] utilized numerical reconstruction methods to obtain MPL microstructure. Experimental characterization of microstructural properties inside an MPL is also a powerful approach for reconstruction. Nanjundappa et al. [11] and Ostadi et al. [12] used a focused ion beam scanning electron microscope (FIB-SEM), while Becker et al. [13] employed 3D tomographical images for microstructure generation and exploration.

Experimental characterization measurements and numerical simulations are the two most common approaches to investigate transport

* Corresponding author.
E-mail address: abel.chuang@ucmerced.edu (P.-Y.A. Chuang).

https://doi.org/10.1016/j.ijhydene.2024.03.102
Received 12 January 2024; Received in revised form 3 March 2024; Accepted 7 March 2024
Available online 14 March 2024
0360-3199/© 2024 The Authors. Published by Elsevier Ltd on behalf of Hydrogen Energy Publications LLC. This is an open access article under the CC BY-NC-ND license (http://creativecommons.org/licenses/by-nc-nd/4.0/).

properties in MPL. Chen et al. [14] used a computed tomography (CT) scanner to characterize fifteen different MPLs, revealing the distribution of porosity and spatial features. Other studies, such as those by Lin et al. [15], Li et al. [16], and Mohseninia et al. [17], also used experimental methods to investigate MPL microstructure and transport properties. In addition to experimental studies, several simulation efforts have been implemented to investigate MPL properties. Lan et al. [18] proposed a simple, fast, and accurate artificial intelligence method, revealing the effects of MPL cracks on fuel cell performance. Specifically, they concluded that the elongated MPL cracks can improve water management, which in turn, enhances fuel cell performance at high current densities. Although it is to be noted that excessive amount of MPL cracks may reduce cell durability [19]. Yang et al. [4] built a 3D GDL with MPL numerical model considering crack shape, porosity, and thickness, and analyzed the effect of cracks on liquid water behavior. Sepe et al. [20] applied the Lattice Boltzmann method (LBM) to simulate liquid water transport in GDL and MPL, providing insights into MPL's effect on liquid water behavior in a fuel cell. In addition, Kulkarni et al. [21] used X-ray CT to characterize PEMFC under compression and obtain the effective properties, Uzundurukan et al. [22] investigated the effects of compression on fuel cell performance both numerically and experimentally, Meng et al. [23] proposed a new nonlinear model to describe the compressive properties. Javaherdeh et al. [24], Lee et al. [25] and Su et al. [26] have deepened understanding of the impact of compression on fuel cell performance.

Although MPL has received less attention compared to GDL and CL, it is indispensable due to its crucial functions. Most MPL studies have primarily focused on liquid water transport [27–32], with fewer exploring the impact of mechanical compression on MPL transport properties [33,34]. Moslemi et al. [35] used multiphase LBM to study the liquid water transport under four different compression levels in the GDL with MPL. Zhang et al. [36] applied pore scale model (PSM) and LBM to study the effect of MPL porosity, mimicking different level of compression, on effective transport properties. None of these studies consider the extrusion deformation of solid particles inside the MPL due to land and channel geometry, therefore, misrepresenting actual MPL properties in realistic operating conditions.

This work aims to bridge the simulation gap and provide an in-depth understanding of the actual effect of mechanical stress on MPL transport properties. The MPL microstructure is reconstructed using numerical simulation, and mechanical stresses are applied to the computational domain using the finite element method (FEM). This study investigates stress-strain-displacement distribution under ten different mechanical compression strains ranging from 0 to 40%, analyzing the variation of microstructural parameters and their impact on effective gas diffusivity, tortuosity, and effective electrical/thermal conductivity using PSM. This research not only offers a novel approach for the mechanical study of MPLs, but also can provide theoretical guidance for future optimization of assembly pressure in fuel cell stacks.

2. Experimental characterization and numerical methods

The present study is divided into four main parts: experimental validation, numerical reconstruction, FEM simulation, and PSM analysis, as illustrated in Fig. 1. The first part is focused on the experimental characterization of MPL material and the objective is to determine the distribution of porosity and pore size, and to obtain SEM characterization images. The purpose of this phase is to establish microstructural parameters for subsequent MPL reconstruction, ensuring the accuracy and reliability of the reconstruction process. Detailed information about this process can be found in our previous work [36]. The second part involves the reconstruction of the MPL using microstructural parameters obtained from the first part. The reconstructed structure is then validated again using SEM images. This numerical reconstruction employs a MATLAB reconstruction code, which initially reconstructs spherical-like carbon particles and then incorporates PTFE into the carbon particle junctions, resulting in a reconstruction close to the actual MPL structure [10].

The third part entails FEM analysis based on explicit dynamics. To more realistically simulate the assembly pressure experienced by the MPL during the assembly of the fuel cell stack, two pieces of structural steel are added to the mechanical compression model. The MPL is compressed and deformed at a specific displacement to study the effect of mechanical compression on the stress-strain-displacement distribution within the MPL. In the fourth part, the deformation geometry model obtained after mechanical compression using FEM is converted to 0, 1, and 2 to represent the pore phases, PTFE, and carbon particles, respectively. This model is then input into the PSM to examine the effect of mechanical compression on effective transport properties. This includes effective gas diffusivity, tortuosity, effective electrical conductivity, and effective thermal conductivity in both in-plane (IP) and through-plane (TP) directions.

2.1. Experimental set-up

Two pieces of experimental equipment used for imaging and elemental characterization: a field emission scanning electron microscope (SEM) and a X-MAX N80 spectrometer JSM-7500F. The MPL microstructure is obtained at two different resolutions from two viewpoints, as shown in Fig. 2.

As mentioned earlier, these images are then compared with those obtained by numerical reconstruction methods to assess the reliability of the reconstructed model. The general porous features of the MPL can be clearly observed from Fig. 2. The carbon particles and PTFE exhibit distinct spherical-like shapes, and these particles have an aggregation phenomenon, forming more pronounced clusters. These apparent

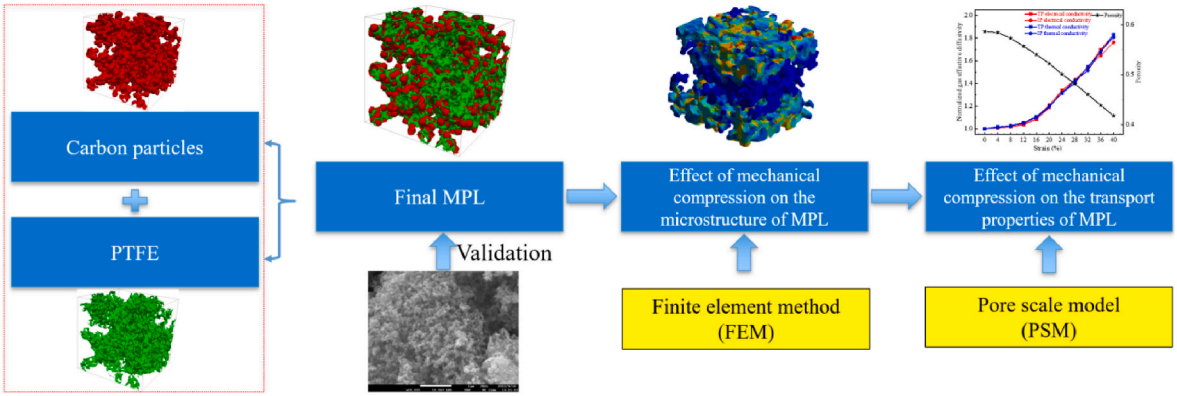

Fig. 1. The process flow of the current study.

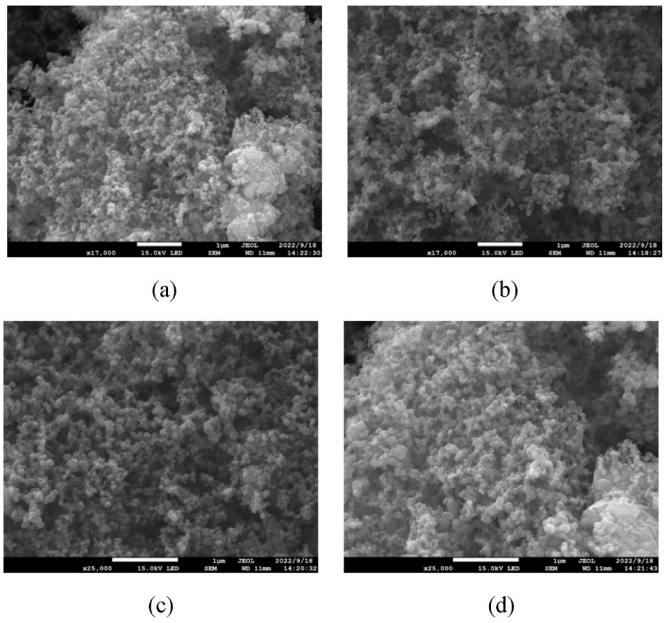

Fig. 2. SEM images of MPL microstructure at different magnifications (a, b) 17,000 × , (c, d) 25,000×.

microstructural features are largely consistent with the reconstructed model obtained throughout numerical reconstruction method, confirming the rationality of the reconstructed model, as depicted in Fig. 3.

2.2. Numerical model

The numerical reconstruction of the MPL is conducted using a custom MATLAB code, comprising two parts: one for the reconstruction of carbon particles and the other for the reconstruction of PTFE additives [36]. The primary input parameters for reconstructing the carbon particle domains include length, width, height, overall porosity, diameter of carbon particles, overlap of carbon spheres, etc. Initially, a multitude of seed particles, individually separated and devoid of contact or overlap, are generated and uniformly dispersed within the predetermined computational domain. Subsequently, the residual carbon particles are introduced into the computational domain, utilizing these seed particles as initiation sites for the stochastic formation of carbon particle agglomerates. The quantity and positioning of the carbon particles undergo iterative adjustments within the reconstruction algorithm until the final porosity attains the predetermined target level. To ensure the viability of the MPL reconstruction process, it is postulated that all carbon particles exhibit spherical geometry with uniform diameters, and the extent of intersection between carbon spheres remains consistent. In the code for PTFE additives, the main input parameter is the weight fraction of PTFE in the entire MPL. The dimensions of the computational domain in this study are 1000 nm × 1000 nm × 1000 nm with a carbon particle diameter of 40 nm and a degree of overlap of 0.25. The obtained carbon particles are shown in Fig. 3(a), with a PTFE weight fraction of 0.35, depicted in Fig. 3(b), and a final MPL porosity of 0.59, shown in Fig. 3(c) [37–41]. As observed in Fig. 3, the carbon particles are spherical, consistent with SEM images, and the agglomerates formed between the carbon spheres bonded by PTFE align with the experimental morphological characterization observed in the SEM. The experimentally measured average pore diameter of MPL is 114 nm and the simulated average pore diameter is 112 nm, with an error of 1.6%. In addition, the maximum error between the simulated and experimental data is 2.73%, which provides the validity of the model. Further details on the validation of internal microstructural properties are provided in our previous work [11,36].

2.3. Finite element method (FEM)

Fig. 4(a) illustrates the use of explicit dynamics for computing the mechanical compression effects on the MPL. In our model, we simulate the compression forces encountered during fuel cell assembly by positioning two pressure plates at the MPL's top and bottom. We set a maximum compression strain of 40%, configuring the computational model to capture data at every 1% increment in compression strain. Subsequently, geometries with different compression strains can be obtained. The MPL's simulation domain is meticulously segmented into 927,351 tetrahedral meshes and 193,922 nodes, as detailed in Fig. 4(b). We have set up node-to-node interactions as frictional contacts with a friction coefficient of 0.30. This setup allows us to accurately simulate the frictional sliding contact between any external node and the scoped entity. Throughout the simulation, we monitor and record changes at each node, ensuring that the interactions remain symmetric across the model. The explicit dynamics equations are used to calculate the relationship between displacement and compression strain using FEM:

$$\delta ij = \frac{(\zeta i,j + \zeta j,i)}{2} \tag{1}$$

where δ is the compression strain, ζ represents the displacement, and the subscripts i, j are spatial vectors.

The relationship between external force and stress is expressed in Eq. (2), while the relationship between stress and strain is expressed in Eqs. (3) and (4), respectively:

$$\gamma ij,j + Fi = \rho\ddot{\zeta} \tag{2}$$

$$\gamma ij = \lambda\sigma kk\gamma jj + 2\mu\sigma ij \tag{3}$$

$$\gamma kk = (3\lambda + 2\mu)\sigma kk = 3E\sigma kk \tag{4}$$

where γ denotes the stress tensor, ρ represents the density, F is the external force, and $\ddot{\zeta}$ is second derivative of displacement with respect to time, referred to as acceleration. λ and μ are constants related to the material properties known as the Lame Constant, γjj is the Kronecker

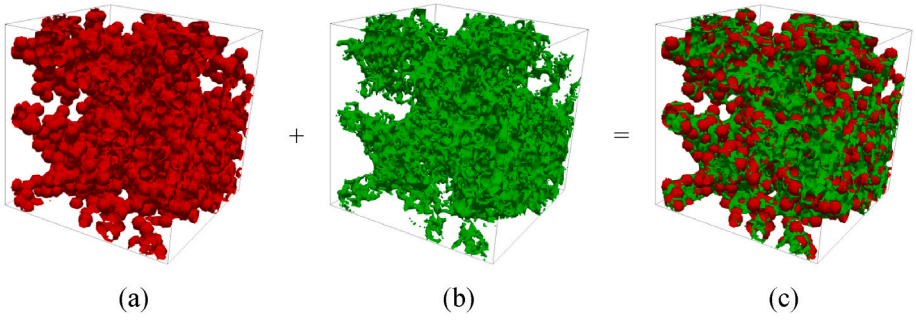

Fig. 3. 3D microstructure rendering of (a) carbon particles, (b) PTFE additives, and (c) the final MPL combining PTFE and carbon particles.

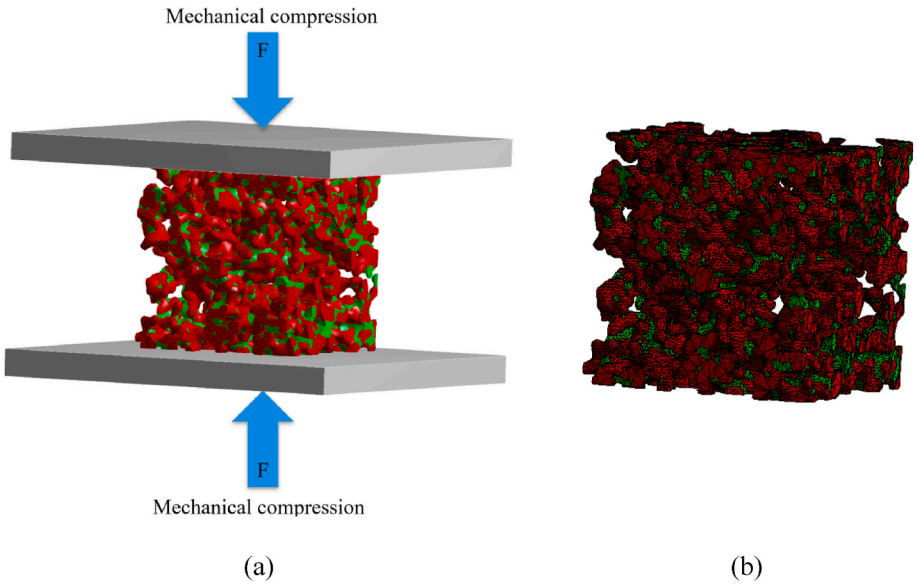

Fig. 4. Finite element analysis for computing the mechanical compression on the MPL: (a) Illustration of mechanical compression, (b) MPL mesh distribution.

symbol and E is the bulk elasticity modulus of MPL materials. In this study, the material of the plates is structural steel, with plate dimensions of 2000 nm × 2000 nm × 150 nm. The material properties for the steel plate, carbon particles, and PTFE additives are provided in Table 1.

The contact type between nodes is solved using the frictional type, as per the following equation:

$$f = \left[\psi d + (\psi s - \psi d)e^{-\beta v}\right]R \tag{5}$$

where f is friction, ψd is dynamic coefficient of friction, ψs is the friction coefficient, β is the exponential decay coefficient, and v is the relative sliding velocity at the point of contact. The fractional coefficient and dynamic coefficient both are set to 0.3 in the FEM. Non-zero values of the dynamic coefficient and decay constant should be used to apply dynamic friction.

2.4. Pore scale model (PSM) and Lattice Boltzmann method (LBM)

The PSM serves as an invaluable tool for enhancing the understanding of fluid flow and transport in porous media, contributing to the design of more efficient and sustainable processes across various scientific and engineering fields. In this study, the MPL, composed of carbon particles and PTFE, functions as a porous medium. PSM is used to calculate the effective gas diffusivity and tortuosity at different mechanical compression strains as well as the effective thermal/electrical conductivity for thermoelectric conduction via solid-phase materials at varying compression strains. Several assumptions in the model are drawn from various literatures [36,42,43].

The effective gas transport and the Knudsen diffusivity can be determined using the following equations [44–46]:

Table 1
Properties of structural steel, carbon particles, and PTFE used in the numerical model.

	Structural steel plate	Carbon particles	PTFE additives
Density (kg m^{-3})	7850	2000	2190
Poisson's ratio	0.30	0.26	0.30
Young's modulus (GPa)	200	100	110
Shear modulus (GPa)	76.9	39.68	42.3
Bulk modulus (GPa)	166.7	69.4	91.66

$$\nabla x_{H_2O} = \frac{RT}{p}\left(\frac{x_{H_2O}j_{O_2} - x_{O_2}j_{H_2O}}{D_{O_2-H_2O}} + \frac{x_{H_2O}j_{N_2} - x_{N_2}j_{H_2O}}{D_{H_2O-N_2}} + \frac{j_{H_2O}}{D_{H_2O,Kn}}\right); \nabla j_{H_2O} = 0 \tag{6}$$

$$\nabla x_{o_2} = \frac{RT}{p}\left(\frac{x_{O_2}j_{H_2O} - x_{H_2O}j_{O_2}}{D_{O_2-H_2O}} + \frac{x_{O_2}j_{N_2} - x_{N_2}j_{O_2}}{D_{O_2-N_2}} + \frac{j_{O_2}}{D_{O_2,Kn}}\right); \nabla j_{O_2} = 0 \tag{7}$$

$$\nabla x_{N_2} = \frac{RT}{p}\left(\frac{x_{N_2}j_{O_2} - x_{O_2}j_{N_2}}{D_{O_2-N_2}} + \frac{x_{N_2}j_{H_2O} - x_{H_2O}j_{N_2}}{D_{H_2O-N_2}} + \frac{j_{N_2}}{D_{N_2,Kn}}\right); \nabla j_{N_2} = 0 \tag{8}$$

$$D_{O_2,Kn} = 4850 d_p \sqrt{\frac{T}{M_{O_2}}} \tag{9}$$

$$D_{N_2,Kn} = 4850 d_p \sqrt{\frac{T}{M_{N_2}}} \tag{10}$$

$$D_{H_2O,Kn} = 4850 d_p \sqrt{\frac{T}{M_{H_2O}}} \tag{11}$$

where x is the mole fraction, j is the flux, D_{i-j} is binary diffusivity, D_{Kn} is Knudsen diffusivity, d_p is the pore diameter, and M is the molecular mass.

The effective electrical and thermal conductivity are solved using ohm's law and Fourier's law in the PSM, as shown in the following equations [47]:

$$j_e = -\sigma_e \nabla \varphi_e; \nabla j_e = 0 \tag{12}$$

$$j_T = -\lambda \nabla T; \nabla j_T = \frac{(\nabla \varphi_e)^2}{\sigma_e} \tag{13}$$

where j is the flux of electrons and heat, σ is conductivity, φ is potential, λ is thermal conductivity. In the computational domain of PSM, the source term of electrons is set as zero, and the source term of heat is generated due to the flow of electrons in the solid phase within the MPL. λ denotes thermal conductivity, encompassing both the solid phases (λ_{solid}) and gas phases (λ_{air}). The λ_{air} is computed by Eq (14):

$$\lambda air = (-0.099489\alpha + 2) \times (0.022423 \times (T - 273.15) + 13.27) \times 10^{-3} \tag{14}$$

$$\alpha = \frac{c_{H_2O}RT}{psat} \tag{15}$$

$$psat = a_1 + a_2(T - 273.15) + a_3(T - 273.15)^2 + a_4(T - 273.153)^3 \tag{16}$$

where α is relative humidity, c_{H_2O} is the molar concentration of water vapor, p_{sat} is the saturation pressure. The coefficient a_1, a_2, a_3 and a_4 in the equation is the constant obtained from fitting curve. $a_1 = -2846.4$, $a_2 = 411.24, a_3 = -10.554$ and $a_4 = 0.16636$.

The thermal conductivities of solid phases are set to be constant in the PSM and are tabulated in Table 2. Additionally, the settings and values of the boundary conditions have been described in detail in our previous work [36].

The governing equations of LBM are as follows

$$\frac{\partial \rho u}{\partial t} + \nabla \cdot \rho u \mu = -\nabla \cdot p + \eta \nabla^2 u + F \tag{17}$$

$$\frac{\partial \varphi}{\partial t} + \nabla \cdot \varphi \mu = M \nabla^2 \mu \tag{18}$$

$$\boldsymbol{f}_i(r + e_i\delta t, t + \delta t) = \boldsymbol{f}_i(r,t) - \boldsymbol{Q}^{-1}\boldsymbol{\Lambda}_f\left(m_f(r,t) - m_f^{eq}(r,t)\right) + \delta t\left(\boldsymbol{I} - \frac{1}{2}\boldsymbol{Q}^{-1}\boldsymbol{\Lambda}_f\boldsymbol{Q}\right)\boldsymbol{G}_i(r,t) \tag{19}$$

$$\boldsymbol{g}_i(r + e_i\delta t, t + \delta t) = \boldsymbol{g}_i(r,t) - \boldsymbol{Q}^{-1}\boldsymbol{\Lambda}_g\left(m_g(r,t) - m_g^{eq}(r,t)\right) \tag{20}$$

where p is pressure , η is viscosity , V refers to the density distribution function at lattice position r and time t, $\boldsymbol{\Lambda}_{a(a=f,g)}$ is the diagonal relaxation matrix, I is the unit matrix.

3. Results and discussions on effects of mechanical compression

3.1. Effect on stress distribution

MPL is more susceptible to plastic deformation or even fragmentation, leading to MEA failure, compared to GDL due to its unique natural mechanical fragility [48–50]. Therefore, studying the stress distribution in the MPL is necessary and critical [51–54]. In the FEM calculation analysis of this study, the mechanical property values of carbon particles and PTFE are assigned separately, consistent with practical cases. Unlike many previous FEM analyses assuming similar properties for different materials, the methodology used in this study enhances the accuracy and reliability of the simulation results. The stress distribution of the MPL and its constituents (carbon particles and PTFE additives) at six different mechanical compression strains (0%, 8%, 16%, 24%, 32% and 40%) is shown in Fig. 5(a). The volume ratio of PTFE to carbon particles in the MPL is approximately 1.0:2.04 and remains the same regardless of the compression strain. However, the volume ratio of the PTFE in the MPL increases with increasing compression stain due to the decrease in void volume. An uncompressed MPL has a volume ratio of PTFE equal to 13.5%. As the compression strain increases to 20% and 40%, the volume ratio of PTFE in MPL increases to 16% and 19.4%, respectively. It is evident from the figures that the stresses in both carbon particles and PTFE gradually increase with increasing mechanical strain. Since the steel structure is the source of the simulated compressive forces, the stresses on the MPL contact surfaces are significantly greater than those in the intermediate regions inside the MPL.

Table 2
Thermal and electrical properties of MPL constituents.

	Carbon particles	PTFE
Thermal conductivity (W m^{-1} K^{-1})	100	0.20
Electrical conductivity (S m^{-1})	15,000	~0

Fig. 5(b) shows the frequency plot of the stress distribution of MPL at ten different mechanical compression strains ranging from 0 to 40%. As seen from the figure, with the increase of mechanical compressive strain, not only does the frequency of larger stresses gradually increase, but the area of stress concentration significantly increases. This is because when the mechanical stress is low, the MPL is only in contact with the structural steel plate through a small portion of the protruding MPL surface, meaning the stress-generating areas only appear above the smaller areas. However, as the mechanical pressure increases, the contact area between the MPL and the structural steel plate increases, as well as the area/frequency of larger stress.

3.2. Effect on strain and displacement distribution

MPLs under compression undergo stress deformation, directly influencing gas-water-thermal-electrical transport properties in the MPLs [34,55]. Therefore, it is essential to analyze the trend of strain displacement with the compression force. The strain distribution for six different compression strains is shown in Fig. 6. A noteworthy observation is the emergence of some red spots in the MPL as the mechanical compression force increases, representing greater strain values. This indicates that particles inside the MPL are not only mechanically compressed but also stretched, resulting in strain values exceeding 1. This is mainly because in this FEM simulation, the mechanical compression force is applied only in the compression direction (Z-direction), while the other four surfaces are set as free boundaries, which resembles the real situation. Under the compression force, some localized particles may experience forces greater than the yield stress of the material, potentially causing deformation or even breakage of carbon and PTFE particles. This phenomena, not observed in previous mechanical stress simulations [36], is successfully demonstrated in the FEM simulation of mechanical stresses in this study. The number and area of these broken particles increase with mechanical compression, concentrating in the region of contact with the structural steel, consistent with the earlier-discussed stress distribution in the MPL.

Since the compression force is only applied in the Z-direction, the displacement of nodes within the MPL occurs mainly in the Z-direction, and the displacements in the X and Y directions are considered negligible [56]. Fig. 7 shows the frequency distribution of displacements of particles inside the MPL in the compression direction at ten different mechanical compressions. As observed from Fig. 7, the displacement along the compression direction inside the MPL is small when the mechanical compression is relatively low, and the frequency distribution of the displacement is mainly around 0. The frequency distribution of displacement of the carbon particles and PTFE inside the MPL increases with the compression strain. As the compression strain increases, the displacements of carbon particles and PTFE inside the MPL increase, and the frequency peaks of the displacements gradually rise. At a compression strain of 20%, there are three displacement peaks in the Z-direction: 0 nm, +80 nm, −80 nm. As the compression strain is further increased to 40%, there becomes two displacement peaks in the Z-direction: +170 nm and −170 nm. This is because as the MPL compression strain increases, the overall pressure inside the MPL becomes larger and relatively more uniform, as shown earlier in Fig. 5(b).

3.3. Effect on the porosity and pore size distribution

Mechanical compression significantly impacts the internal microstructure of MPL, particularly the internal porosity and pore size distribution [6,34,53,54,57,58]. Fig. 8 illustrates the porosity and pore size distribution for ten different compression strains as well as the average MPL porosity as a function of the compression strain. It is observed that with the increase in mechanical compression, both the MPL thickness in the compression direction and the overall porosity decrease. The initial porosity of the reconstructed MPL is approximately 0.58 when the MPL is not subjected to any mechanical compression. As the mechanical

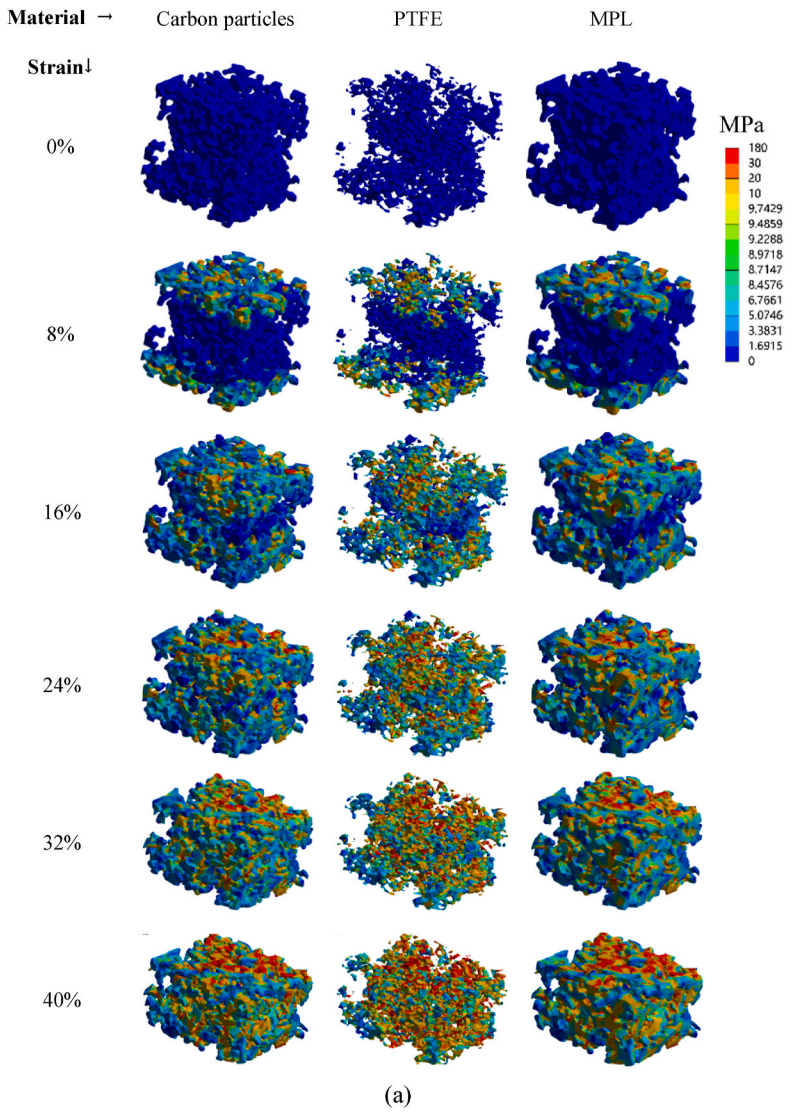

Fig. 5. (a) Stress distribution in MPL at different mechanical compression strains, (b) Intensity distribution of MPL at different compression strains.

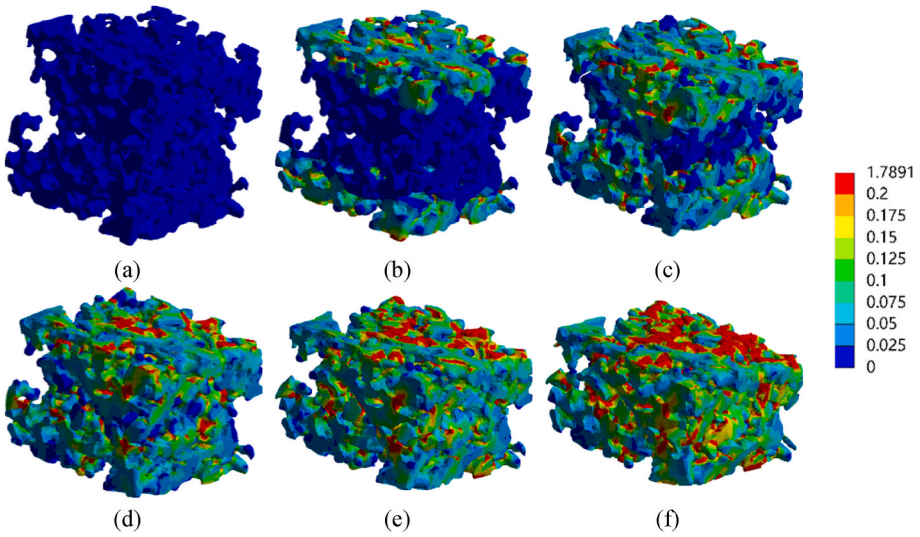

Fig. 6. Strain distribution in MPL at different mechanical compression strains of (a) 0%, (b) 8%, (c) 16%, (d) 24%, (e) 32%, (f) 40%.

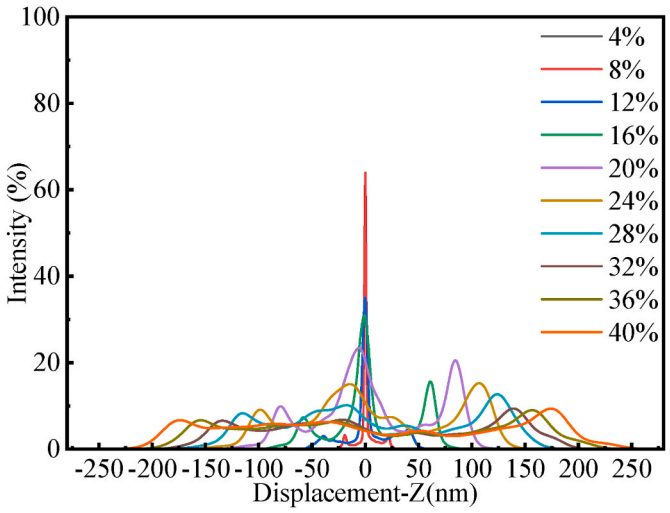

Fig. 7. Displacement profiles for Z-displacement in MPL at different mechanical compression strains.

compression strain increases to 20%, the porosity decreases to 0.52, and with further mechanical compression to 40%, the porosity decreases to 0.42.

The simulated average porosity of the MPL under compression is compared with the empirical results shown in Fig. 8(c). For the empirical formula, it is assumed that the effect of mechanical compression on porous media is elastic, and that compression only reduces the pore volume [59,60]. However, the actual situation is not ideal. The solid-phase materials in mechanical compression occur between the interpenetration, material destruction, and so on. Therefore, the actual porosity under mechanical compression is greater than the porosity obtained by the empirical formula in the ideal situation as shown in Fig. 8(c). The pore size distribution also significantly decreases with the increase in compression strain. When there is no compression force on the MPL, the average pore size is approximately 50 nm, and the size of the largest pore is ~120 nm. As the compression strain increases to 20%, the average pore size reduces to ~40 nm, with the largest pore size at around 90 nm. With further compression strain, the average pore size decreases to about 30 nm, with the largest pore size at ~70 nm. The 40% mechanical compression strain almost reduces the average pore size inside the MPL by 40% and the maximum pore size by about half. This further supports the necessity of an in-depth study of the effect of mechanical stress on the microstructure inside the MPL.

3.4. Effect on the gas diffusivity and permeability

The effect of mechanical compression on tortuosity and effective gas transport in both the in-plane (IP) and through-plane (TP) directions in the MPL is shown in Fig. 9(a). As observed, the compression effect on MPL tortuosity is pronounced and nearly identical in both directions, further confirming the isotropy of the MPL. MPL tortuosity shows a significant increase with compression strain. When compression strain increases from 0 to 20%, tortuosity increases by 25%. As compressive strain increases from 20% to 40%, tortuosity further increases by 60%, representing an extreme 2.4 times increment compared to the prior increase. A compression strain of 20% appears to be a critical cut-off point for the sensitivity of the mechanical pressure's effect on MPL tortuosity and effective gas diffusivity. Below 20% compression strain, the impact on MPL's internal transport properties is not particularly noticeable. The effective gas diffusivity decreases by 30% with an increase in mechanical compressive strain from 0 to 20%. As the strain increases from 20% to 40%, the effective gas diffusivity decreases by 57%, nearly twice the change observed when the strain is increased from 0 to 20%.

In addition, the effect of mechanical compression on permeability in both the IP and TP directions in the MPL are also studied as shown in Fig. 9(b). The IP and TP permeability decreases almost linearly with increasing compression ratio due to decreasing pore size. These noteworthy findings related to transport in the MPL align well with previous research and underscores the significance of selecting an appropriate compression force during the assembly of a fuel cell stack [8,60–63].

3.5. Effect on electrical and thermal conductivity

Thermo-electrical conduction within an MPL predominantly occurs through carbon particles. When the MPL undergoes mechanical compression, the contact area between the carbon particles changes, influencing the effective electrical and thermal conductivities in the MPL. The impact of mechanical compression on effective thermal and electrical conductivity in both the IP and TP directions is depicted in Fig. 10. As the mechanical compression strain increases from 0 to 40%, the MPL porosity decreases from 0.58 to 0.42, and the effective electrical and thermal conductivity exhibit nearly identical trends under this strain change. This is attributed to the fact that the majority of heat and electricity within the MPL are conducted by carbon particles. Under mechanical compression, the nodes between solid-phase materials

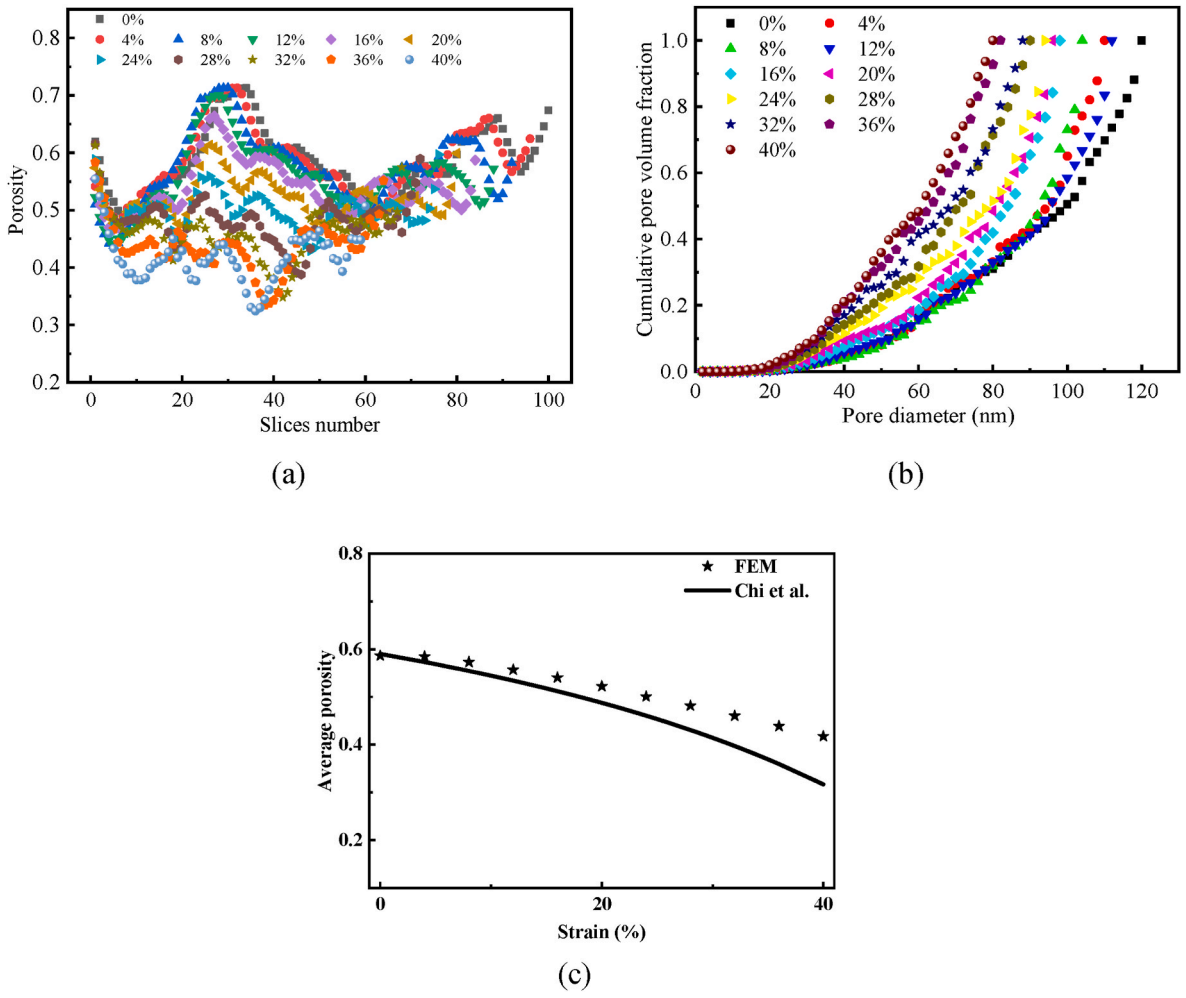

Fig. 8. Distribution of microstructural parameters: (a) porosity and (b) pore size, and (c) average porosity at different mechanical compression strains.

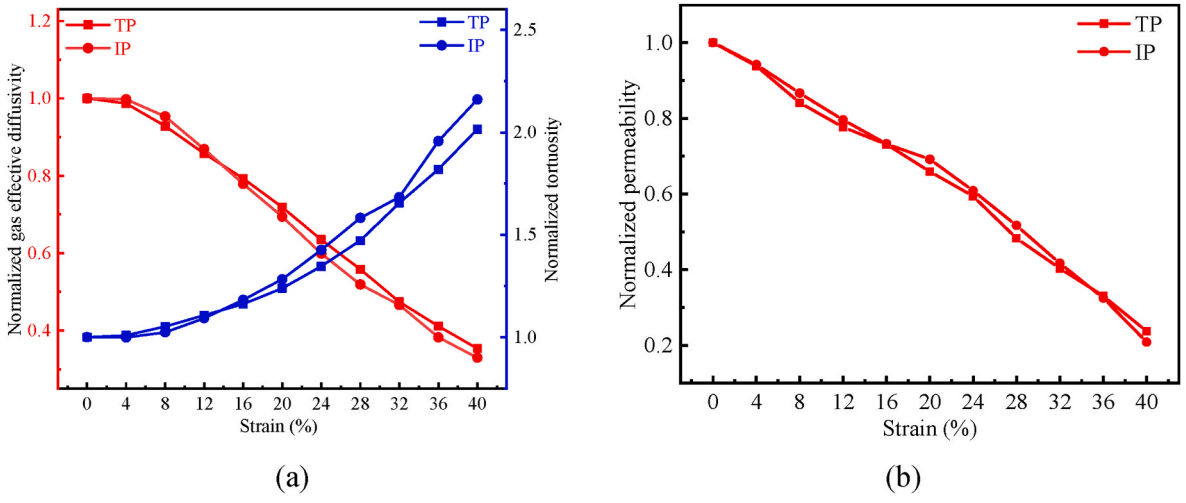

Fig. 9. The effect of mechanical compression strain on (a) normalized gas effective diffusivity and tortuosity and (b) normalized permeability in the TP and IP directions.

deform due to compression, resulting in almost identical changes in effective electrical and thermal conductivities, both increasing with mechanical compressive strain, consistent with previous findings [36,62,64,65]. Additionally, the similarity of heat and electricity in both the IP and TP directions confirms the isotropy of the MPL.

The MPL was reconstructed assuming both carbon particles and PTFE as spherical, leading to almost identical thermoelectric conduction properties in different directions, a key reason for the MPL's isotropy. This inherent property aligns well with actual situation observed from previous study [66].

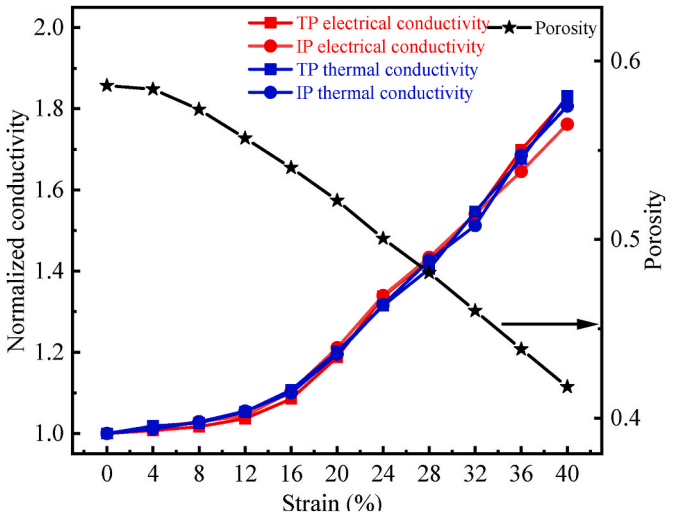

Fig. 10. Normalized electrical and thermal conductivity in the TP and IP directions under different mechanical compression strains.

When the mechanical compression strain increases from 0 to 40%, the MPL conductivity increases by 1.8 times. Meanwhile, conductivity increases by 20% as the mechanical compression strain rises from 0 to 20%. However, with a further increase from 20% to 40%, conductivity increases by 50%, which is 2.5 times the conductivity induced by the initial 20% change in compression strain, similar to the change observed in effective gas diffusivity in the previous section. A mechanical compression strain of about 20% is again a critical point. This intriguing finding contributes to the theoretical basis for the optimization of future fuel cell assembly load design.

4. Conclusions

In this study, a numerical reconstruction method is used to reconstruct the MPL microstructure, incorporating spherical carbon particles and PTFE additives to emulate real material and structure. The accuracy of the reconstruction is validated by comparing the resulting porosity and pore size distribution with SEM images. In the subsequent stage, FEM is implemented to simulate the mechanical compression process on the MPL. Explicit dynamic is utilized to calculate the MPL compression under mechanical compression strain ranging from 0 to 40%. Notably, the carbon particles and PTFE within the MPL are assigned their respective physical properties, significantly enhancing the precision of the FEM simulation.

The key findings of this study indicate that the stress values within the MPL escalate with increasing compression strain, leading to a larger stress concentration area. Nevertheless, the stress distribution becomes more uniform, and the maximum stress value within the MPL occurs on the surface in the TP direction. The trend of strain and displacement in the MPL under mechanical pressure is similar to that of stress, with strain and displacement both increasing with mechanical pressure, particularly at the MPL surface. The displacement distribution shows an overall increase with compression strain, displaying a more uniform distribution. Concurrently, both porosity and pore size distribution decrease with increased mechanical compression. When the mechanical compression strain rises from 0 to 40%, the porosity decreased by 29%, and the average pore size decreases by 40%, from approximately 50 nm to about 30 nm. Moreover, the study reveals that effective gas diffusivity decreases by 60%, tortuosity rises by 100%, and effective conductivity increases by 80% as the mechanical compression strain increases from 0 to 40%. In sum, a mechanical compression strain of 20% emerges as a critical point where the transport properties within the MPL exhibit relatively marginal changes. Beyond 20% compression strain, the alterations in transport properties become more pronounced.

This study presents an innovative method for simulating mechanical compression, which significantly improves the accuracy and reliability of calculations. Not only does it quantify the impact of mechanical stresses within the MPL on its transport properties, but it also establishes a theoretical foundation for optimizing the assembly force in fuel cell stacks to enhance overall fuel cell performance.

Declaration of competing interest

The authors declare that they have no known competing financial interests or personal relationships that could have appeared to influence the work reported in this paper.

Acknowledgements

This work was supported by National Natural Science Foundation of China (grant numbers 52306270); the Guangdong Basic and Applied Basic Research Foundation (grant number 2022A1515110456); Donghai Laboratory Open-end Fund, Zhoushan, China (grant number DH-2022KF0305); the research innovation team construction plan of Wuhan City Polytechnic College (grant number 2023whcvcTD01).

References

[1] Majlan EH, Rohendi D, Daud WRW, Husaini T, Haque MA. Electrode for proton exchange membrane fuel cells: a review. Renew Sustain Energy Rev 2018;89:117–34.
[2] Sui P-C, Zhu X, Djilali N. Modeling of PEM fuel cell catalyst layers: status and outlook. Electrochem Energy Rev 2019;2:428–66.
[3] Ryan EM, Mukherjee PP. Mesoscale modeling in electrochemical devices—a critical perspective. Prog Energy Combust Sci 2019;71:118–42.
[4] Yu Y, Chen S, Wei H. Numerical study on the effect of microporous layer crack changes on water management in gas diffusion layer of proton exchange membrane fuel cell. Int J Heat Mass Tran 2023:212.
[5] Yin Q, Gao W, Zhang C, Gong F, Tu Z, Li Y, et al. The buffer microporous layer improved water management for proton exchange membrane fuel cell at varying humidification. J Electroanal Chem 2023:928.
[6] Zhang J, Wang B, Jin J, Yang S, Li G. A review of the microporous layer in proton exchange membrane fuel cells: materials and structural designs based on water transport mechanism. Renew Sustain Energy Rev 2022;156:111998.
[7] Wu Y, Garg S, Li M, Idros MN, Li Z, Lin R, et al. Effects of microporous layer on electrolyte flooding in gas diffusion electrodes and selectivity of CO2 electrolysis to CO. J Power Sources 2022:522.
[8] Zhang H, Rahman MA, Mojica F, Sui PC, Chuang PYA. A comprehensive two-phase proton exchange membrane fuel cell model coupled with anisotropic properties and mechanical deformation of the gas diffusion layer. Electrochim Acta 2021;382:138273.
[9] Deng H, Hou Y, Jiao K. Lattice Boltzmann simulation of liquid water transport inside and at interface of gas diffusion and micro-porous layers of PEM fuel cells. Int J Heat Mass Tran 2019;140:1074–90.
[10] El Hannach M, Singh R, Djilali N, Kjeang E. Micro-porous layer stochastic reconstruction and transport parameter determination. J Power Sources 2015;282:58–64.
[11] Nanjundappa A, Alavijeh AS, El Hannach M, Harvey D, Kjeang E. A customized framework for 3-D morphological characterization of microporous layers. Electrochim Acta 2013;110:349–57.
[12] Ostadi H, Rama P, Liu Y, Chen R, Zhang XX, Jiang K. 3D reconstruction of a gas diffusion layer and a microporous layer. J Membr Sci 2010;351:69–74.
[13] Becker J, Wieser C, Fell S, Steiner K. A multi-scale approach to material modeling of fuel cell diffusion media. Int J Heat Mass Tran 2011;54:1360–8.
[14] Chen Y-C, Karageorgiou C, Eller J, Schmidt TJ, Büchi FN. Determination of the porosity and its heterogeneity of fuel cell microporous layers by X-ray tomographic microscopy. J Power Sources 2022;539.
[15] Lin R, Yu X, Chen L, Tang S, Yin X, Hao Z. Structure majorization on the surface of microporous layer in polymer electrolyte membrane fuel cells to optimize performance and durability. Energy Convers Manag 2021;243:114319.
[16] Li B, Xie M, Ji H, Chu T, Yang D, Ming P, et al. Optimization of cathode microporous layer materials for proton exchange membrane fuel cell. Int J Hydrogen Energy 2021;46:14674–86.
[17] Mohseninia A, Kartouzian D, Eppler M, Langner P, Markötter H, Wilhelm F, et al. Influence of structural modification of micro-porous layer and catalyst layer on performance and water management of PEM fuel cells: hydrophobicity and porosity. Fuel Cell 2020;20:469–76.
[18] Lan S, Lin R, Dong M, Lu K, Lou M. Image recognition of cracks and the effect in the microporous layer of proton exchange membrane fuel cells on performance. Energy 2023:266.

[19] Mehrazi S, Sarker M, Mojica F, Rolfe P, Chuang P-YA. A rheological approach to studying process-induced structural evolution of the microporous layer in a proton exchange membrane fuel cell. Electrochim Acta 2021;389:138690.
[20] Sepe M, Satjaritanun P, Zenyuk IV, Tippayawong N, Shimpalee S. The impact of micro porous layer on liquid water evolution inside PEMFC using lattice Boltzmann method. J Electrochem Soc 2021;168:074507.
[21] Kulkarni N, Cho JIS, Jervis R, Roberts EPL, Francesco I, Kok MDR, et al. The effect of non-uniform compression on the performance of polymer electrolyte fuel cells. J Power Sources 2022:521.
[22] Uzundurukan A, Bilgili M, Devrim Y. Examination of compression effects on PEMFC performance by numerical and experimental analyses. Int J Hydrogen Energy 2020;45:35085–96.
[23] Meng L, Zhou P, Yan Y, Guo D. Compression properties of gas diffusion layers and its constitutive model under cyclic loading. Int J Hydrogen Energy 2021;46:15965–75.
[24] Javaherdeh K, Moslemi M, Ashorynejad HR. Liquid water phenomena in compressed gas diffusion and micro-porous layers of Proton exchange membrane fuel cell. Heat Mass Tran 2023;59:489–508.
[25] Lee S-H, Kim HM. Effects of rib structure and compression on liquid water transport in the gas diffusion layer of a polymer electrolyte membrane fuel cell. J Mech Sci Technol 2022:1–12.
[26] Su ZY, Liu CT, Chang HP, Li CH, Huang KJ, Sui PC. A numerical investigation of the effects of compression force on PEM fuel cell performance. J Power Sources 2008;183:182–92.
[27] Sarker M, Rahman MA, Mojica F, Mehrazi S, Kort-Kamp WJM, Chuang P-YA. Experimental and computational study of the microporous layer and hydrophobic treatment in the gas diffusion layer of a proton exchange membrane fuel cell. J Power Sources 2021;509:230350.
[28] Naito H, Ishikawa K, Sasabe T, Hirai S, Tanuma T. Investigation of effects of hydrophilic micro-porous layer on liquid water behavior by X-ray imaging. J Power Sources 2021;507:230285.
[29] Ira Y, Bakhshan Y, Khorshidimalahmadi J. Effect of wettability heterogeneity and compression on liquid water transport in gas diffusion layer coated with microporous layer of PEMFC. Int J Hydrogen Energy 2021;46:17397–413.
[30] Fontana M, Ramos R, Morin A, Dijon J. Direct growth of carbon nanotubes forests on carbon fibers to replace microporous layers in proton exchange membrane fuel cells. Carbon 2021;172:762–71.
[31] Hou Y, Li X, Du Q, Jiao K, Zamel N. Pore-scale investigation of the effect of micro-porous layer on water transport in proton exchange membrane fuel cell. J Electrochem Soc 2020;167:144504.
[32] Simon C, Endres J, Nefzger-Loders B, Wilhelm F, Gasteiger HA. Interaction of pore size and hydrophobicity/hydrophilicity for improved oxygen and water transport through microporous layers. J Electrochem Soc 2019;166:F1022–35.
[33] Song K, Wang Y, Ding Y, Xu H, Mueller-Welt P, Stuermlinger T, et al. Assembly techniques for proton exchange membrane fuel cell stack: a literature review. Renew Sustain Energy Rev 2022;153.
[34] Shi Q, Feng C, Ming P, Tang F, Zhang C. Compressive stress and its impact on the gas diffusion layer: a review. Int J Hydrogen Energy 2022;47:3994–4009.
[35] Moslemi M, Javaherdeh K, Ashorynejad HR. Effect of compression of microporous and gas diffusion layers on liquid water transport of PEMFC with interdigitated flow field by Lattice Boltzmann method. Colloids Surf A Physicochem Eng Asp 2022:642.
[36] Zhang H, Shao X, Zhan Z, Sarker M, Sui P-C, Chuang P-YA, et al. Pore-scale modeling of microporous layer for proton exchange membrane fuel cell: effective transport properties. Membranes 2023;13:219.
[37] Mohseninia A, Eppler M, Kartouzian D, Markötter H, Kardjilov N, Wilhelm F, et al. PTFE content in catalyst layers and microporous layers: effect on performance and water distribution in polymer electrolyte membrane fuel cells. J Electrochem Soc 2021:168.
[38] Öztürk A, Fıçıcılar B, Eroğlu İ, Bayrakçeken Yurtcan A. Facilitation of water management in low Pt loaded PEM fuel cell by creating hydrophobic microporous layer with PTFE, FEP and PDMS polymers: effect of polymer and carbon amounts. Int J Hydrogen Energy 2017;42:21226–49.
[39] Sadeghifar H, Djilali N, Bahrami M. Effect of Polytetrafluoroethylene (PTFE) and micro porous layer (MPL) on thermal conductivity of fuel cell gas diffusion layers: modeling and experiments. J Power Sources 2014;248:632–41.
[40] Molaeimanesh GR, Akbari MH. Impact of PTFE distribution on the removal of liquid water from a PEMFC electrode by lattice Boltzmann method. Int J Hydrogen Energy 2014;39:8401–9.
[41] Park S, Lee J-W, Popov BN. Effect of PTFE content in microporous layer on water management in PEM fuel cells. J Power Sources 2008;177:457–63.
[42] Zhu L, Zhang H, Xiao L, Bazylak A, Gao X, Sui P-C. Pore-scale modeling of gas diffusion layers: effects of compression on transport properties. J Power Sources 2021;496:229822.
[43] Zhang H, Zhu L, Harandi HB, Duan K, Zeis R, Sui P-C, et al. Microstructure reconstruction of the gas diffusion layer and analyses of the anisotropic transport properties. Energy Convers Manag 2021;241:114293.
[44] Lange KJ, Sui P-C, Djilali N. Pore scale modeling of a proton exchange membrane fuel cell catalyst layer: effects of water vapor and temperature. J Power Sources 2011;196:3195–203.
[45] Hao L, Cheng P. Lattice Boltzmann simulations of water transport in gas diffusion layer of a polymer electrolyte membrane fuel cell. J Power Sources 2010;195:3870–81.
[46] Sui PC, Djilali N, Wang Q. A pore scale model for the transport phenomena in the catalyst layer of a PEM fuel cell. Micro/Nanoscale Heat Transfer International Conference. 2008.
[47] Lange KJ, Sui P-C, Djilali N. Pore scale simulation of transport and electrochemical reactions in reconstructed PEMFC catalyst layers. J Electrochem Soc 2010;157:B1434.
[48] Chan C, Zamel N, Li X, Shen J. Experimental measurement of effective diffusion coefficient of gas diffusion layer/microporous layer in PEM fuel cells. Electrochim Acta 2012;65:13–21.
[49] Burheim OS, Su H, Pasupathi S, Pharoah JG, Pollet BG. Thermal conductivity and temperature profiles of the micro porous layers used for the polymer electrolyte membrane fuel cell. Int J Hydrogen Energy 2013;38:8437–47.
[50] Unsworth G, Zamel N, Li X. Through-plane thermal conductivity of the microporous layer in a polymer electrolyte membrane fuel cell. Int J Hydrogen Energy 2012;37:5161–9.
[51] Zhang Z, He P, Dai Y-J, Jin P-H, Tao W-Q. Study of the mechanical behavior of paper-type GDL in PEMFC based on microstructure morphology. Int J Hydrogen Energy 2020;45:29379–94.
[52] Millichamp J, Mason TJ, Neville TP, Rajalakshmi N, Jervis R, Shearing PR, et al. Mechanisms and effects of mechanical compression and dimensional change in polymer electrolyte fuel cells – a review. J Power Sources 2015;284:305–20.
[53] Chun JH, Jo DH, Kim SG, Park SH, Lee CH, Kim SH. Improvement of the mechanical durability of micro porous layer in a proton exchange membrane fuel cell by elimination of surface cracks. Renew Energy 2012;48:35–41.
[54] Kusoglu A, Karlsson AM, Santare MH, Cleghorn S, Johnson WB. Mechanical behavior of fuel cell membranes under humidity cycles and effect of swelling anisotropy on the fatigue stresses. J Power Sources 2007;170:345–58.
[55] Liu Q, Lan F, Chen J, Zeng C, Wang J. A review of proton exchange membrane fuel cell water management: membrane electrode assembly. J Power Sources 2022;517:230723.
[56] Xu J, Zhu L, Xiao L, Hu H, Yin Z, Zhang R, et al. A multiscale study on the effect of compression on lithium-ion battery separators. J Energy Storage 2022;54.
[57] Bao Y, Wang Z, Gan Y. Numerical investigation of compressive stress and wettability effects on fluid transport in polymer electrolyte membrane fuel cell porous layers. Energy Technol 2022;10.
[58] Serincan MF, Pasaogullari U. Effect of gas diffusion layer anisotropy on mechanical stresses in a polymer electrolyte membrane. J Power Sources 2011;196:1314–20.
[59] Chi PH, Chan SH, Weng FB, Su A, Sui PC, Djilali N. On the effects of non-uniform property distribution due to compression in the gas diffusion layer of a PEMFC. Int J Hydrogen Energy 2010;35:2936–48.
[60] Zhang H, Xiao L, Chuang P-YA, Djilali N, Sui P-C. Coupled stress–strain and transport in proton exchange membrane fuel cell with metallic bipolar plates. Appl Energy 2019;251:113316.
[61] Xiao L, Luo M, Zhang H, Zeis R, Sui P-C. Solid mechanics simulation of reconstructed gas diffusion layers for PEMFCs. J Electrochem Soc 2019;166:F377–85.
[62] Mason TJ, Millichamp J, Neville TP, El-kharouf A, Pollet BG, Brett DJL. Effect of clamping pressure on ohmic resistance and compression of gas diffusion layers for polymer electrolyte fuel cells. J Power Sources 2012;219:52–9.
[63] Xing XQ, Lum KW, Poh HJ, Wu YL. Optimization of assembly clamping pressure on performance of proton-exchange membrane fuel cells. J Power Sources 2010;195:62–8.
[64] Movahedi M, Ramiar A, Ranjber AA. 3D numerical investigation of clamping pressure effect on the performance of proton exchange membrane fuel cell with interdigitated flow field. Energy 2018;142:617–32.
[65] Tanaka S, Bradfield WW, Legrand C, Malan AG. Numerical and experimental study of the effects of the electrical resistance and diffusivity under clamping pressure on the performance of a metallic gas-diffusion layer in polymer electrolyte fuel cells. J Power Sources 2016;330:273–84.
[66] Shojaeefard MH, Molaeimanesh GR, Nazemian M, Moqaddari MR. A review on microstructure reconstruction of PEM fuel cells porous electrodes for pore scale simulation. Int J Hydrogen Energy 2016;41:20276–93.